International Journal of Heat and Fluid Flow 30 (2009) 186–197

Contents lists available at ScienceDirect

International Journal of Heat and Fluid Flow

journal homepage: www.elsevier.com/locate/ijhff

Numerical simulations of anisothermal laminar vortex rings with large density variations

S. Benteboula [a,*], G. Lauriat [b]

[a] UPMC Univ Paris 06, UMR 7598, Laboratoire Jacques-Louis Lions, 175, rue de Chevaleret, F-75005 Paris, France
[b] Université Paris-Est, Marne-la-Vallée, Laboratoire de Modélisation et Simulation Multi Echelle (MSME FRE CNRS 3160), F-77454 Marne-la-Vallée Cedex 2, France

ARTICLE INFO

Article history:
Received 24 December 2007
Received in revised form 11 December 2008
Accepted 15 December 2008
Available online 23 February 2009

Keywords:
Numerical simulation
Anisothermal vortex ring
Low Mach number flow
Variable properties

ABSTRACT

A numerical investigation of anisothermal ideal gas flows generated during the injection phase in a combustion chamber is presented. Impulsive and brief time injection cases with a piston stroke $L_p = 4$ are simulated for fairly large Reynolds numbers (Re = 750 and 1500). The dynamics of the jet flow are characterised by large density gradients due to temperature variations. A computational code based on a non-divergence free, fractional-step method has been developed for solving the 3D, time-dependent Navier–Stokes and energy equations in cylindrical coordinates. The problem formulation is based on the low Mach number approximation for non reactive flows with variable physical properties. Simulations of the injection of hot or cold fluid into a stagnant environment are performed for a wide range of the jet-to-ambient density ratio, $\alpha = \rho_j/\rho_a$. For hot jets, the results show that the temperature and the density in the leading vortex are close to that of the initially injected hot fluid, whereas they are intermediate between the ambient and the injected fluid ones in the case of cold jets. Furthermore, the overall characteristics of the vortex such as circulation, impulse and kinematics are strongly dependent on the density ratio. Their values are larger for the cold jets and conversely smaller for the hot jets.

1. Introduction

The main feature appearing during the fuel discharge through a circular opening, orifice or nozzle, is the formation of a leading vortex ring followed by a trailing jet. This topic is of great interest either from a fundamental point of view or from industrial applications concern. Engineering processes using injection systems, such as combustion in automobile and aeronautical engines, are illustrative examples. One must recall that the process of combustion involving fluid mechanics, heat and mass transfer and chemistry is extremely complex. When all these phenomena are accounted for, in industrial codes aiming at simulating combustion, the accuracy of the flow solutions are often affected especially the vortex characteristics.

In a laboratory, the vortex ring is obtained with a piston-cylinder mechanism by pushing a column of fluid through an orifice or a tube. The boundary layers of the fluid ejected through the orifice or the nozzle edge separate and roll up into a vortex ring. Once the injection is stopped, the vortex ring detaches and travels downstream induced by its own momentum. During its displacement, the vortex grows by entrainment of the surrounding fluid and by viscous diffusion. For long-duration injections, Kelvin–Helmholtz instabilities may develop in the trailing layer with more vortex interactions.

In the case of constant density flows, vortex rings have been extensively studied theoretically and experimentally. For a general review on the generation, formation, evolution and interaction of vortex rings, the reader could refer to Shariff and Leonard (1992) and Lim and Nickels (1995). Concerning theories, there are two models that describe the vortex ring formation. The first model (Saffman, 1978; Pullin, 1979) relies on similarity theory. It predicts the following evolution laws for the dimensionless circulation, vortex core diameter, axial position and radius of the vorticity centroid, respectively, in the injection phase as:

$$\Gamma \sim t^{1/3}, \quad \delta_v \sim t^{1/3}, \quad Z_v \sim t^{2/3}, \quad R_v \sim t^{2/3}.$$

The second model, the so-called 'slug-flow', estimates the vortex characteristics, circulation, impulse and energy, using only the piston's velocity evolution given by the following dimensionless relationships:

$$\Gamma(t) = \frac{1}{2}\int_0^t V_p^2(\tau)d\tau, \quad I = \frac{\pi}{4}\int_0^t V_p^2(\tau)d\tau, \quad E = \frac{\pi}{8}\int_0^t V_p^3(\tau)d\tau.$$

James and Madnia (1996) investigated numerically the effects of different geometrical configurations (orifice and nozzle) and velocity evolutions on the vortex ring characteristics. For the post-formation phase, they found that the total circulation varied as $\Gamma \sim t^{-0.33}$,

* Corresponding author. Present address: CEA Saclay, DM2S/SFME/LTMF, 91191 Gif sur Yvette Cedex, France.
E-mail addresses: benteboula@ann.jussieu.fr (S. Benteboula), lauriat@univ-mlv.fr (G. Lauriat).

0142-727X/$ - see front matter © 2008 Elsevier Inc. All rights reserved.
doi:10.1016/j.ijheatfluidflow.2008.12.013

Nomenclature

D_j^*	orifice diameter
e	internal energy per unit mass
g'	reduced gravity
I	dimensionless hydrodynamic impulse
k	dimensionless thermal conductivity
L_p	dimensionless piston stroke
L_r, L_z	dimensionless width and length of the computational domain
Ma	Mach number, $Ma = V_j^*/c^*$
Pr	Prandtl number, $Pr = \mu_j^* C_p^*/k_j^*$
p	dimensionless pressure, $p = p^*/r^*\rho_j^* T_j^*$
rand	Random function
Re	Reynolds number $Re = \rho_j^* V_j^* D_j^*/\mu_j^*$
(r, θ, z)	dimensionless radial, azimuthal and axial coordinates $r = r^*/D_j^*,\ z = z^*/D_j^*$
t	dimensionless time, $t = t^* V_j^*/D_j^*$
T	dimensionless temperature, $T = T^*/T_j^*$
U_v	dimensionless vortex velocity
V_j^*	maximum of the inflow velocity
V_p^*	piston velocity
$\mathbf{v}$	dimensionless velocity vector
(v_r, v_θ, v_z)	radial, azimuthal and axial dimensionless velocities

Greeks

α	density or temperature ratio, $\alpha = \rho_j^*/\rho_a^* = T_a^*/T_j^*$
δ_ω	dimensionless vorticity thickness
δ_v	dimensionless vortex core radius
Γ	dimensionless total circulation
γ	specific heat ratio, $\gamma = C_p^*/C_v^*$
μ	dimensionless dynamic viscosity, $\mu = \mu^*/\mu_j^*$
ω	dimensionless vorticity
ρ	dimensionless density, $\rho = \rho^*/\rho_j^*$
σ	exponent in the viscosity law (Eq. (9))

Superscripts

$(\cdot)^*$	dimensional quantities

Subscripts

$(\cdot)_j$	jet variables
$(\cdot)_a$	ambient flow variables

which confirms the experimental data by Maxworthy (1977) and Didden (1979). However, recent experiments by Dabiri and Gharib (2004) showed different scales law $\Gamma \sim t^x$ with $x \in [-0.27, -0.15]$. The existence of a universal time scale for the vortex ring formation was proved by Gharib et al. (1998). For an impulsive and long-time injection (piston stroke $L_p \in [4, 12]$), they observed that the axisymmetric leading vortex pinches-off from the trailing jet stem for a formation time $t_F \in [3.6, 4.5]$. Simulations carried out by Benteboula (2006) for the incompressible vortex ring by imposing $\rho_j = \rho_a$ with $L_p = 6$ showed results in agreement with Gharib's results. A scale law for the circulation, $\Gamma = t^{-0.22}$, and a time formation, $t_F = 3.6$, were obtained. Zhao et al. (2000) studied the interaction between the trailing jet instability and the leading vortex ring. They showed that, for a long-time discharge, this interaction accelerates the process of pinch-off and has a significant effect on the vortex ring circulation.

Despite their importance in industrial applications such as, ignition problems, few results are available in the open literature about the variable density vortex rings, in particular the influences of the jet-to-ambient density ratio, α, on the flow variables and vortex characteristics. As reported in Iglesias et al. (2005), the leading vortex ring could privilege the molecular mixing process which takes place at diffusion scales (see Verzicco and Orlandi, 1995). To the best of our knowledge, there is only a brief recent communication by Iglesias et al. (2005) in which the authors suggested a 'slug-flow' model to estimate circulation of variable density vortex rings. They assumed an inviscid fluid and uniform velocity at the entry equal to that of the piston. One drawback of this model is that the evolution of circulation depends on a vortex velocity which is not known a priori.

Variable density flows occurring at low Mach number are encountered in several physical phenomena ranging from natural convection, ocean circulations driven by salinity and density gradients, aeroacoustics, air–fuel combustion to open fires. For such flows, an asymptotic formulation of the Navier–Stokes equations was proposed by Majda and Sethian (1985), amongst others. This formulation which is intermediate between the compressible and incompressible Navier–Stokes equations was initially applied to solve combustion problems with premixed flames.

From a numerical point of view, there are two main approaches in the development of algorithms for low Mach number flows. The first consists of modifications based on reduction of the Mach number for compressible (density-based) solvers (see Turkel, 1987; Guillard and Viozat, 1999; Roller and Munz, 2000). It deals with flows ranging from supersonic to low Mach number regime and aeroacoustics. The foremost difficulty here arises from the large differences between the acoustic and the advective scales. This stiffness is discussed in Turkel (1987). It should be noted that computations using fully compressible Navier–Stokes equations with explicit methods would require very small time-steps for matching stability conditions when $Ma \to 0$, which make them unsuitable for computing industrial flows. In the second approach, as adopted in this work, the incompressible (pressure-based) algorithms (projection method, SIMPLE) are extended to the non-divergence free velocity flows. These algorithms are well adapted to incompressible flows as well as to flows with variable density (Klein, 1995), irrespective of the pressure fluctuations. By applying the low Mach number approximation to the Navier–Stokes equations, acoustic waves are removed while entropy and vorticity modes as well as compressibility due to exothermic chemical reactions can still be described. In these conditions, large density variations due to thermal effects are allowed, for instance, in combustion. This approach has been used in different ways. Some authors (Pember et al., 1996; Nicoud, 2000; Munz et al., 2003) solved, for the projection step, a Poisson equation with variable coefficients and an explicit expression for the velocity divergence on the right-hand side. The second class of algorithms considers a Poisson equation with constant coefficients and a right-hand side including density variations, see Cook and Riley (1996), Najm et al. (1998) and Benteboula (2006).

In the present study we consider a variable density and viscosity flow resulting from injection of a gas at temperature T_j and density ρ_j into an initially quiescent atmosphere at a different temperature T_a and density ρ_a. This subject is investigated numerically for a wide range of the jet-to-ambient density ratios, α. The mathematical model used is the 3D Navier–Stokes and energy equations based on a low Mach number approximation. The injection velocity is assumed to be small enough for the flow to be considered laminar with large density variations.

The main objectives of the present work were, on one hand, to develop a numerical algorithm able to handle strong density gradients through the jet-to-ambient density ratio, α, for flows involving

high temperature gradients such as combustion initiated by a hot reactive jet. On the other hand, we aimed at analyzing the influence of density ratio on the jet flow dynamics, thermals and integral characteristics of the vortex ring for both hot and cold fluid injections. The present paper is organized as follow. In Section 2, we introduce the mathematical model of the Navier–Stokes equations within the framework of a low Mach number assumption. In Section 3, we describe the numerical procedure used to integrate the governing equations.. In the last section, results of variable density vortex rings simulations for different ratios α are discussed for both hot and cold jets. These simulations are compared to the reference case of an incompressible vortex ring ($\alpha = 1$) obtained for $\rho_j = \rho_a$.

2. Governing equations

In this study, the jet flow with variable properties, density, viscosity and thermal conductivity, is governed by the three-dimensional unsteady Navier–Stokes equations formulated in the low Mach number approximation.

First, the fully compressible Navier–Stokes equations written in the conservative form are nondimensionalized by using the reference quantities associated to the injected fluid: $D_j^*, V_j^*, \rho_j^*, T_j^*$. In this work, the Froude number $Fr = V_j^*/\sqrt{g\prime D_j^*}$ is assumed large enough for neglecting the buoyancy forces within the computational domain.

Next, all the primitive variables of the flow are expanded in power series law of a small parameter $\epsilon = \gamma Ma^2 \ll 1$

$$\rho = \rho_0 + \gamma Ma^2 \rho_1 + \mathcal{O}((\gamma Ma^2)^2) \tag{1}$$

$$\mathbf{v} = \mathbf{v}_0 + \gamma Ma^2 \mathbf{v}_1 + \mathcal{O}((\gamma Ma^2)^2) \tag{2}$$

$$T = T_0 + \gamma Ma^2 T_1 + \mathcal{O}((\gamma Ma^2)^2) \tag{3}$$

$$p = p_0 + \gamma Ma^2 p_1 + \mathcal{O}((\gamma Ma^2)^2) \tag{4}$$

$$\rho e = \frac{p_0}{\gamma - 1} + \gamma Ma^2 \frac{p_1}{\gamma - 1} + \gamma Ma^2 \rho_0 \frac{\mathbf{v}_0^2}{2} + \mathcal{O}((\gamma Ma^2)^2) \tag{5}$$

To derive the low Mach number equations, primitive variables are substituted by their expansions in the fully compressible Navier–Stokes equations and the lowest order terms in γMa^2 are collected. We consider here that the low Mach number flow is fully described by the convective space and time scales. Thus, the single scale asymptotic analysis (see Müller, 1998) leads to the following equations:

at the order -1, the momentum equations reduce to

$$\nabla p_0 = 0 \tag{6}$$

At the order zero, we obtain the following low Mach number, dimensionless governing equations:

– continuity equation

$$\frac{\partial \rho_0}{\partial t} + \nabla \cdot (\rho_0 \mathbf{v}_0) = 0 \tag{7}$$

– momentum equations

$$\frac{\partial (\rho_0 \mathbf{v}_0)}{\partial t} + \nabla \cdot (\rho_0 \mathbf{v}_0 \otimes \mathbf{v}_0) = -\nabla p_1 + \frac{1}{Re} \nabla \cdot \bar{\bar{\tau}}_0 \tag{8}$$

The shear stress tensor $\bar{\bar{\tau}}_0$ for a Newtonian fluid is given by

$$\bar{\bar{\tau}}_0 = -\frac{2}{3}\mu(\nabla \cdot \mathbf{v}_0) \cdot \bar{\bar{I}} + \mu(\nabla \mathbf{v}_0 + \nabla^t \mathbf{v}_0)$$

In the present study, the temperature viscosity variation is approximated by the following power law:

$$\mu = T_0^\sigma \quad \text{with } \sigma \approx 0.5 \tag{9}$$

– evolution equation of the density

$$\frac{\partial \rho_0}{\partial t} + \mathbf{v}_0 \cdot \nabla \rho_0 = -\frac{1}{T_0}\left[\frac{1}{RePr} \nabla \cdot (\mu \nabla T_0)\right] \tag{10}$$

The specific heat C_p and Prandtl number being assumed constant, the dimensionless thermal conductivity is replaced by the dimensionless viscosity (i.e $k^*/k_j^* = \mu^*/\mu_j^*$).It should be noted that Eq. (10), commonly employed in combustion studies (see, for example, Cook and Riley (1996)), is obtained by combining the energy and continuity equations and by using the equation of state. Another form of the energy equation can be written in term of temperature (see Boersma et al., 1998; Najm et al., 1998).

– equation of state for an ideal gas

$$p_0 = \rho_0 T_0 = 1 \tag{11}$$

The most important outcome of the low Mach number approximation is the splitting of the pressure into two components; a thermodynamic pressure p_0 constant in space according to Eq. (6) and allowed to vary in time, and a dynamic pressure p_1 decoupled from density and temperature fluctuations. Since we are considering an open computational domain, the thermodynamic pressure p_0 is also constant in time.

In the next subsection, subscripts "0" related to the zero-order approximation will be kept only for the pressure in order to differentiate its zero- and first-order components.

2.1. Low Mach number equations in cylindrical coordinates

The Navier–Stokes equations to be discretized are formulated in cylindrical coordinates (r, θ, z) for the set of conservative variables $(\rho, \rho q_r, \rho v_\theta, \rho v_z, p)$ where $q_r = r v_r$, as used in Verzicco and Orlandi (1996). It follows:

– continuity equation

$$\frac{\partial \rho}{\partial t} + \frac{1}{r}\frac{\partial (\rho v_\theta)}{\partial \theta} + \frac{1}{r}\frac{\partial (\rho q_r)}{\partial r} + \frac{\partial (\rho v_z)}{\partial z} = 0 \tag{12}$$

– density evolution equation

$$\frac{\partial \rho}{\partial t} + \left[\frac{v_\theta}{r}\frac{\partial \rho}{\partial \theta} + \frac{q_r}{r}\frac{\partial \rho}{\partial r} + v_z \frac{\partial \rho}{\partial z}\right] = -\frac{1}{RePr}\frac{1}{T}\left[\frac{1}{r^2}\frac{\partial}{\partial \theta}\left(\mu \frac{\partial T}{\partial \theta}\right) + \frac{1}{r}\frac{\partial}{\partial r}\left(r\mu \frac{\partial T}{\partial r}\right) + \frac{\partial}{\partial z}\left(\mu \frac{\partial T}{\partial z}\right)\right] \tag{13}$$

– momentum equations

$$\frac{\partial}{\partial t}(\rho q_r) + \frac{\partial}{\partial r}\left(\frac{q_r}{r}\rho q_r\right) + \frac{\partial}{\partial \theta}\left(\frac{v_\theta}{r}\rho q_r\right) + \frac{\partial}{\partial z}(v_z \rho q_r) - v_\theta \rho v_\theta = -r\frac{\partial p_1}{\partial r} + \frac{1}{Re}\left[\frac{\partial}{\partial r}(r\tau_{rr}) + \frac{\partial}{\partial \theta}(\tau_{\theta r}) + r\frac{\partial}{\partial z}(\tau_{zr}) - \tau_{\theta\theta}\right] \tag{14}$$

$$\frac{\partial}{\partial t}(\rho v_\theta) + \frac{1}{r^2}\frac{\partial}{\partial r}(r q_r \rho v_\theta) + \frac{1}{r}\frac{\partial}{\partial \theta}(v_\theta \rho v_\theta) + \frac{\partial}{\partial z}(v_z \rho v_\theta) = -\frac{1}{r}\frac{\partial p_1}{\partial \theta} + \frac{1}{Re}\left[\frac{1}{r^2}\frac{\partial}{\partial r}(r^2 \tau_{r\theta}) + \frac{1}{r}\frac{\partial}{\partial \theta}(\tau_{\theta\theta}) + \frac{\partial}{\partial z}(\tau_{z\theta})\right] \tag{15}$$

$$\frac{\partial}{\partial t}(\rho v_z) + \frac{1}{r}\frac{\partial}{\partial r}(q_r \rho v_z) + \frac{1}{r}\frac{\partial}{\partial \theta}(v_\theta \rho v_z) + \frac{\partial}{\partial r}(v_z \rho v_z) = -\frac{\partial p_1}{\partial z} + \frac{1}{Re}\left[\frac{1}{r}\frac{\partial}{\partial r}(r\tau_{rz}) + \frac{1}{r}\frac{\partial}{\partial \theta}(\tau_{\theta z}) + \frac{\partial}{\partial z}\tau_{zz}\right] \tag{16}$$

– equation of state for a perfect gas

$$p_0 = \rho T = 1 \tag{17}$$

2.1.1. Initial and boundary conditions

At the initial time $t = 0$, we assume that the density and temperature fields in the quiescent ambient are uniform ($\rho = \rho_a = 1/\alpha, T = T_a = \alpha$). Moreover, the dynamic pressure and

all the velocities are set equal to zero which implies that the unknowns: $\rho q_r = \rho v_\theta = \rho v_z = p_1 = 0$.

2.1.2. Inflow boundary $z = 0$

At the orifice, $0 \leqslant r < 0.5$, the following injection conditions are applied to generate the vortex ring:

$$(\rho q_r) = 0, \quad (\rho v_\theta) = 0, \quad (\rho v_z)(r,t) = f(r)g(t),$$

where $f(r)$ is a top hat jet profile that approximates the profiles measured experimentally as proposed by Michalke (1984) and used by several authors (see James and Madnia, 1996; Zhao et al., 2000), is defined by

$$f(r) = \frac{1}{2}\left\{1 - \tanh\left[\frac{1}{\delta}\left(r - \frac{1}{2}\right)\right]\right\}. \tag{18}$$

In Eq. (18) $\delta = D_j^*/(2\Theta_j^*)$ is the jet parameter and Θ_j^* the momentum thickness of the inlet profile. The injection program $g(t)$ is the function that controls the inflow velocity in time (James and Madnia, 1996) given by

$$g(t) = \begin{cases} \frac{1}{2} + \frac{1}{2}\tanh\left(\frac{5}{\tau_1}(t - \tau_1)\right), & t < \tau_1, \\ \frac{1}{2} + \frac{1}{2}\tanh\left(\frac{5}{\tau_1}(\tau_1 + \tau_2 - t)\right), & t > \tau_1 + \frac{\tau_2}{2}. \end{cases} \tag{19}$$

For an impulsive and brief injection, $\tau_1 = 0.01$ and $\tau_2 = 4$ were used in Eq. (19). The density at the orifice is parametrized by the jet-to-ambient density ratio $\alpha = \rho_j/\rho_a$

$$\rho(r,t) = \rho_a[1 + (\alpha - 1)f(r)g(t)]. \tag{20}$$

2.1.3. Outflow boundary $z = L_z$

The dependent variables ρq_r, ρv_θ and ρv_z in the momentum equations satisfy the one-dimensional convection equation (Orlanski, 1976)

$$\frac{\partial X}{\partial t} + C\frac{\partial X}{\partial z} = 0, \tag{21}$$

where $C = 0.5$ is a phase speed. Note that the value of C does not affect the solution because the velocities at the outlet are corrected at each time-step to insure mass conservation.

For the density, we apply a Neumann condition at the domain exit $\partial\rho/\partial z = 0$.

2.1.4. Axis $r = 0$

Symmetry conditions for the flow variables are applied at $r = 0$, except for the radial component ρq_r which is equal zero per definition

$$\frac{\partial \rho}{\partial r} = 0, \quad \frac{\partial \rho v_\theta}{\partial r} = 0, \quad \frac{\partial \rho v_z}{\partial r} = 0 \quad \text{and} \quad \rho q_r = 0.$$

2.1.5. Lateral boundary $r = L_r$

Neumann conditions for the density and fluxes are applied

$$\frac{\partial \rho}{\partial r} = 0, \quad \frac{\partial \rho v_\theta}{\partial r} = 0, \quad \frac{\partial \rho q_r}{\partial r} = 0 \quad \text{and} \quad \frac{\partial \rho v_z}{\partial r} = 0.$$

These conditions allow the entrainment of fluid through the lateral boundary. In the θ direction, periodicity is imposed on all variables.

3. Numerical procedure

From a mathematical viewpoint, the low Mach number formulation is similar to that for incompressible flows, since the density in the momentum equations does not depend on the dynamic pressure p_1. Therefore, the numerical procedure may be based on fractional-step methods usually implemented in incompressible (pressure-based) solvers. The method employed here is an extension to the low Mach number regime with a non divergence-free velocity ($\nabla \cdot \mathbf{v} \neq 0$). Four algorithms (see Benteboula, 2006), all of them being based on the projection method and using different time integration schemes, have been implemented and tested: 1. second-order explicit Adams–Bashforth scheme for both density and momentum equations, 2. semi-implicit predictor–corrector scheme, 3. first-order Euler scheme for density and second-order semi-implicit Adams–Bashforth/Crank–Nicholson scheme for momentum, 4. first-order Euler scheme for density and second-order explicit Adams–Bashforth for momentum. Since each of these algorithms showed order of time accuracy within the range [1.58–1.61], the most efficient version (4.) in terms of CPU-time requirements is presented in what follows.

3.1. Spatial discretization

The computational domain is covered with a staggered three-dimensional cylindrical grid, the fluxes and velocities being located at the centers of the faces and, the scalar variables ρ, T, p at the center of the cells. A centered finite-difference scheme with a second-order accuracy was retained for the spatial discretization. However, it was necessary to use a total variation diminishing scheme (TVD) introduced by Harten (1983) for the convective terms in the energy equation (Eq. (10)), as in Vreugenhil and Koren (1993). To this end, the advective term $\mathbf{v} \cdot \nabla\rho$ is reformulated as

$$\mathbf{v} \cdot \nabla\rho = \nabla \cdot (\rho\mathbf{v}) - \rho\nabla \cdot \mathbf{v}$$

The TVD scheme is applied only to the conservative part $\nabla \cdot (\rho\mathbf{v})$. This scheme appears to be necessary for high density ratios α in order to damp the spurious oscillations introduced by the centered treatment of the advection. The space order of accuracy, in region of discontinuity, is reduced to one. In the region of smooth solutions sufficiently far from the critical points the scheme is second-order accurate. The overall accuracy is then less than two.

3.2. Time integration

The evolution equation of the density (Eq. (13)) is firstly integrated with a first-order Euler scheme

$$\frac{\rho^{n+1} - \rho^n}{\Delta t} = \left(-A_\rho + D_\rho\right)^n$$

where A_ρ and D_ρ are the convective and diffusive terms, respectively, given by

$$A_\rho = \nabla \cdot (\rho\mathbf{v}) - \rho \cdot \nabla\mathbf{v}, \quad D_\rho = -\frac{1}{T}\left[\frac{1}{RePr}\nabla \cdot (\mu\nabla T)\right]$$

A second-order backward scheme is then employed for approximating the time derivative in the continuity equation. It reads

$$\left(\frac{\partial\rho}{\partial t}\right)^{n+1} = \frac{3\rho^{n+1} - 4\rho^n + \rho^{n-1}}{2\Delta t}$$

This term is generally an instability source for such an algorithm, as reported in Nicoud (2000) and Cook and Riley (1996).

Next, the momentum equations, written in the conservative form, are advanced in time with a fractional-step method by using a second-order explicit Adams–Bashforth scheme. The resolution consists in two main steps:

1. *Prediction*: in this step, an intermediate solution $\widehat{\rho v_c}$ is computed as

$$\frac{\widehat{\rho\mathbf{v}}_c - \rho^n\mathbf{v}_c^n}{\Delta t} = -\nabla p^n + \frac{3}{2}(-A_c + C_c + D_c)^n - \frac{1}{2}(-A_c + C_c + D_c)^{n-1}$$

where $\mathbf{v}_c = (r v_r, v_\theta, v_z)$ and A_c, C_c, D_c are the advective terms, coupled viscous terms and second-order derivatives viscous terms, respectively.

2. *Projection*: in order to satisfy the mass conservation, the following Poisson equation for the variable Φ was solved:

$$\Delta\Phi^{n+1} = \frac{1}{\Delta t}\left[\nabla\cdot\widehat{\rho v}_c + \left(\frac{\partial\rho}{\partial t}\right)^{n+1}\right].$$

Φ is related to the pressure by $\nabla\Phi^{n+1} = \nabla(p^{n+1} - p^n)$.

The pressure gradient is next updated with the following relation $\nabla p^{n+1} = \nabla p^n + \nabla\Phi^{n+1}$.

The velocity field at step $(n+1)$ are then obtained from the correction equation

$$(\rho\mathbf{v}_c)^{n+1} - \widehat{\rho\mathbf{v}}_c = -\Delta t\nabla\Phi^{n+1}$$

Finally, the temperature distribution is deduced from the equation of state for an ideal gas, $T^{n+1} = 1/\rho^{n+1}$, and the viscosity field from the power law $\mu^{n+1} = (T^{n+1})^\sigma$.

3.3. Mesh convergence

A mesh convergence study was performed by using uniform grids for the following set of parameters: $L_r \times L_z = 3 \times 7$, $t = 6$, $\alpha = 1/4$, $Re = 1500$. Since large density and velocity gradients occur in the radial direction, the grid was progressively refined in the r-direction, starting from a quite coarse mesh ($N_r = 100$). The cells number in the streamwise direction was fixed to $N_z = 500$, which was found large enough. The results for the maximum values of the axial and radial velocities presented in Table 1 show that converged solutions may be assumed reached for a 350×500 mesh. Note that the value of axial velocity for 100×500 cells showed that the cell sizes were too large to properly capture variations in the radial direction. In order to reduce the CPU-time consumption for a given accuracy, a non-uniform mesh based on the results reported in Table 1 was then used. A hyperbolic tangent function in the radial direction, which provides a dense grid distribution around $r = 0.5$, was thus applied. As can be seen in Table 1, the maxima in velocity components may be accurately calculated by using a non-uniform grid with $N_r = 200$ only. This grid was then used for most of the computations discussed in the present paper.

The time-step considered for stability conditions was such that the CFL-condition was met according to the mesh size. For the chosen non-uniform mesh 200×500, Table 2 shows that the results are in good agreement. Therefore, $\Delta t = 10^{-3}$ was used to cover the range of the density ratios to be simulated.

3.4. Validation

Comparisons of incompressible vortex ring solutions were conducted: first, with the experimental measurements of Gharib et al. (1998), second with the numerical predictions of Zhao et al. (2000). The numerical simulations were performed for an impulsive and long-time injection ($L_p = 6$) and for $Re = 3100$. The results for the temporal evolution of the total circulation, which gives information of the amount of vorticity in the flow field, and vortex ring circulation are shown in Fig. 1. The total circulation is calculated by using the following expression:

Table 2
Maximum values of the streamwise and crosswise velocities versus the time-step.

Δ t	2×10^{-3}	10^{-3}	5×10^{-4}
v_z	0.95160	**0.95124**	0.95103
v_r	0.53909	**0.53907**	0.53900

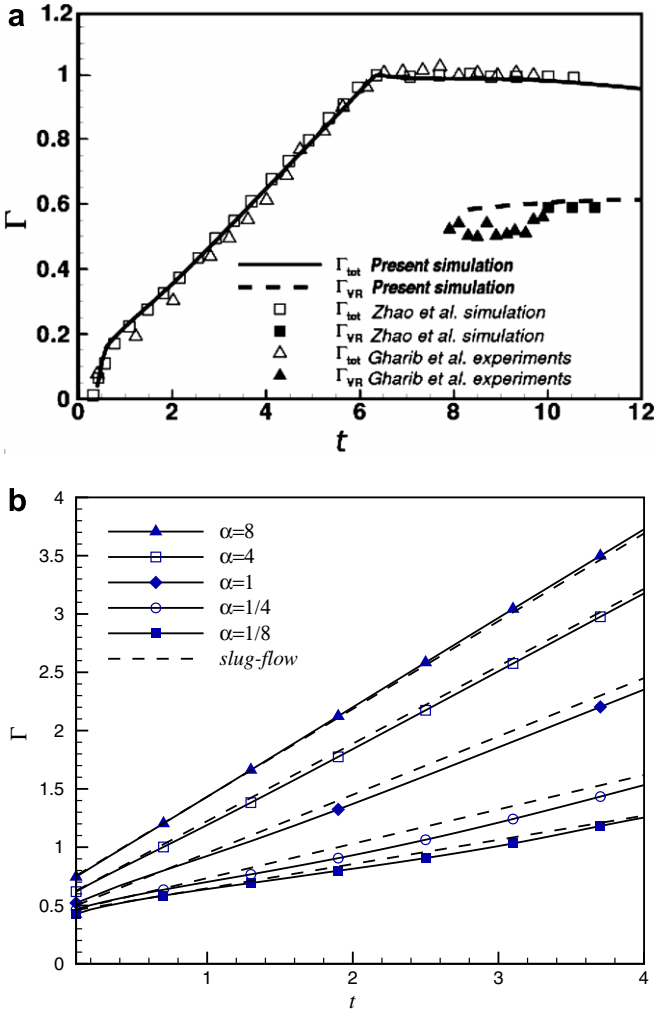

Fig. 1. (a) Comparison between the present simulations for $\alpha = 1$, Zhao et al. (2000) simulations and Gharib et al. (1998) experiments for incompressible starting jets with $Re = 3100$, $L_p = 6$. (b) Temporal evolutions of the total circulation for different density ratios compared to the prediction of the slug-flow model.

$$\Gamma = \int_0^{L_z}\int_0^{L_r} \omega_\theta\, dr\, dz \tag{22}$$

Since the flow is axisymmetric, only the circumferential component of the vorticity, given by $\omega_\theta = \partial v_r/\partial z - \partial v_z/\partial r$, is nonzero.

As can be seen, the present simulations are in good agreement both with the computations of Zhao et al. (2000) and experiments of Gharib et al. (1998). It is worth recalling how is predicted the circulation for incompressible flows by using the so-called slug-flow

Table 1
Maximum values of the streamwise and crosswise velocities versus the grid points.

Mesh	100×500	150×500	200×500	250×500	300×500	350×500	$\mathbf{200_{var} \times 500}$
v_z	0.96007	0.94635	0.94651	0.94865	0.95052	0.95123	**0.95124**
v_r	0.57508	0.55022	0.54188	0.54087	0.53988	0.53922	**0.53907**

Table 3
Vortex velocities at $t = 2$ for different α-ratios.

Density ratio, α	1/8	1/4	1/2	1	2	4	8
Front velocity, U_v	0.2795	0.3589	0.3838	0.4667	05625	0.6571	0.7658

model. This model concerns the vortex ring generated by a piston-cylinder mechanism and attempts to link the circulation to the injection process through Eq. (22) (Glezer, 1988; Shariff and Leonard, 1992). The velocity at the orifice exit is assumed to be equal to the piston velocity and the vorticity in this region is approached by $\omega_\theta = -\partial v_z/\partial r$. It follows that:

$$\frac{d\Gamma}{dt} = \int_0^\infty \omega_\theta v_z dr \approx \int_0^\infty -v_z \frac{\partial v_z}{\partial r} dr = \frac{1}{2} V_p^2(t).$$

$$\text{So, } \Gamma(t) = \frac{1}{2}\int_0^t V_p^2(\tau) d\tau.$$

In order to generalize the estimation of the total circulation for variable density vortex rings, the slug-flow model was extended by Iglesias et al. (2005). The result is

$$\Gamma = \frac{1}{2} + \frac{t}{2}\left[1 + U_v^2(1-\alpha)\right].$$

It should be noted that this model require a prior knowledge of the vortex velocity U_v which is assumed to be constant. Nevertheless, this quantity computed in a post-processing step was not found constant, especially for hot jets. Hence, the front jet velocities at instant $t = 2$, corresponding approximately to the half-time of the injection program at which the vortex velocities start to stabilize, were used (see Table 3).

The comparison with the slug-flow model plotted in Fig. 1 shows a rather good agreement although this model overestimates the circulation values for hot jets, especially as the density ratio decreases. The discrepancies between the curves is partly due to non-constant hot jets velocities and to the contribution of the radial component of the velocity which is neglected in the slug-flow model.

4. Results and discussion

The simulations presented in this section were carried out for both three-dimensional and axisymmetric flows. The computational domain is a cylinder of radius $L_r = 3$ and length $L_z = 7$, in which the fluid is injected through an orifice of radius $r_j = 0.5$ located at the center of the entry section. The injection velocity program provided a piston stroke $L_p = 4$. The cylinder is discretized with a grid of $N_\theta \times N_r \times N_z = 32 \times 200 \times 500$ cells. For the axisymmetric simulations, N_θ is assigned to $N_\theta = 1$. We considered Reynolds numbers of $Re = 750$, 1000, 1500. In all the cases, the Prandtl number is kept constant, $Pr = 0.7$. To investigate the effect of the jet-to-ambient density ratio on the flow field, a broad range of α varying from 1 to 8 for cold jets and, from 1/8 to 1 for hot jets was explored. The simulations were also compared to the incompressible case corresponding to $\alpha = 1$. Note that flows with strong density gradients are more difficult to compute. Thus, calculations with $\alpha = 1/8$ require more refined grids in the axial direction: we used $N_z = 600$. For $\alpha = 8$, a smaller time-step have been used ($\Delta t = 5.10^{-4}$) because the jet penetration is about three times faster than for hot jets. To describe the long-time behavior of a hot jet slowed by a denser surroundings, the dimensionless integration time have been extended up to $t = 40$ for $\alpha = 1/8$.

4.1. Three-dimensional simulations

Fig. 2a shows a three-dimensional simulation of a vortex ring produced by an impulsively started cold jet ($\alpha = 2$). In this simulation, the axisymmetric profile defined in Eq. (18) is imposed on the axial flux (ρv_z) for a long-time discharge with a shut-off time of the velocity program $t = 4.02$. Surfaces of constant temperature $T = 1.05, 1.35, 1.65$ are illustrated at different times during and following the injection phase. It can be seen in Fig. 2a a roll up of the shear layer that leads to the formation of a toroidal vortex ring at the head of the flow followed by a symmetric jet stem. The vortex ring is propelled by the momentum imparted during the injection phase and grows by entrainment of the surrounding fluid and by viscous diffusion which becomes dominant after injection is stopped. Thermal contours take similar shapes to the vortex ring.

In order to highlight three-dimensional effects of the jet flow, a random perturbation of small amplitude was applied to the spatial profile (Eq. (18)) at the orifice exit in the circumferential direction of the form $f_p(r) = f(r) + A_z r\cos(m\theta + 2\pi\text{rand}(0))$, where A_z and m are the perturbation amplitude and mode, respectively. Fig. 2b shows the surfaces of constant vorticity $\omega_\theta = -3, 1.8, 3.5$ and density $\rho = 0.55, 0.65, 0.8$ for a hot jet ($\alpha = 1/2$). Apart from the fact that a leading vortex is generated in an almost similar way as described above, the plots demonstrate how the resulting sheet of vorticity is distorted by this perturbation which is shed in the flow field. Hence, the loss of symmetry is also apparent on the trailing jet.

4.2. Axisymmetric simulations

4.2.1. Vorticity fields

The instantaneous contours of the azimuthal vorticity in the plane (r, z) are represented in Fig. 3 for the post-formation phase at the same dimensionless time $t = 10$ for hot jets $\alpha = (1/8, 1/4)$, isothermal jet $\alpha = 1$ (incompressible) and cold jets $\alpha = (4, 8)$. We see that the common feature of all these cases is the formation of the leading vortex at the head of the flow. Plots show that the colder the fluid, the faster the jet is progressing. In the case of hot jets, the roll-up of vorticity sheets is more intense and additional vortices are created in the jet stem. The core diameter of the leading vortex becomes smaller as the temperature of the injected fluid is raised. Furthermore, we observe the development of a negative vorticity layer (shown by dashed lines) at the head of the vortex as well as in the jet stem. This counter-rotation is due to the baroclinic torque that acts in regions of variable density and leads to the acceleration of the pinch-off process, whereas the cold jet has a larger leading vortex with large momentum which assists its penetration. Consequently, the vortex ring grows considerably by thermal diffusion when its vorticity decreases, as can be seen for $\alpha = 8$. At $t = 10$, the vortex is thus already leaving the computational domain. It should be noted that the negative vorticity near the inlet section is due to the formation of the stopping vortex, as already mentioned in James and Madnia (1996).

The radial variations of the streamwise velocity v_z and azimuthal vorticity ω_θ are shown in Fig. 4. These plots are extracted along a line crossing the vortex center (region of maximum vorticity) for the five injection cases displayed in Fig. 3 Even if the injection is stopped at $t = 4.02$, the velocity profiles of the cold and isothermal jets reach values higher than the maximum of the injection velocity ($v_j = 1$) at a radial position corresponding to the orifice lip. These increases in the axial velocity are due to the superposition of rotation and injection. As the flow develops in the radial direction, negative velocities are seen at larger distances from the symmetry axis as the density ratio increases. It can also

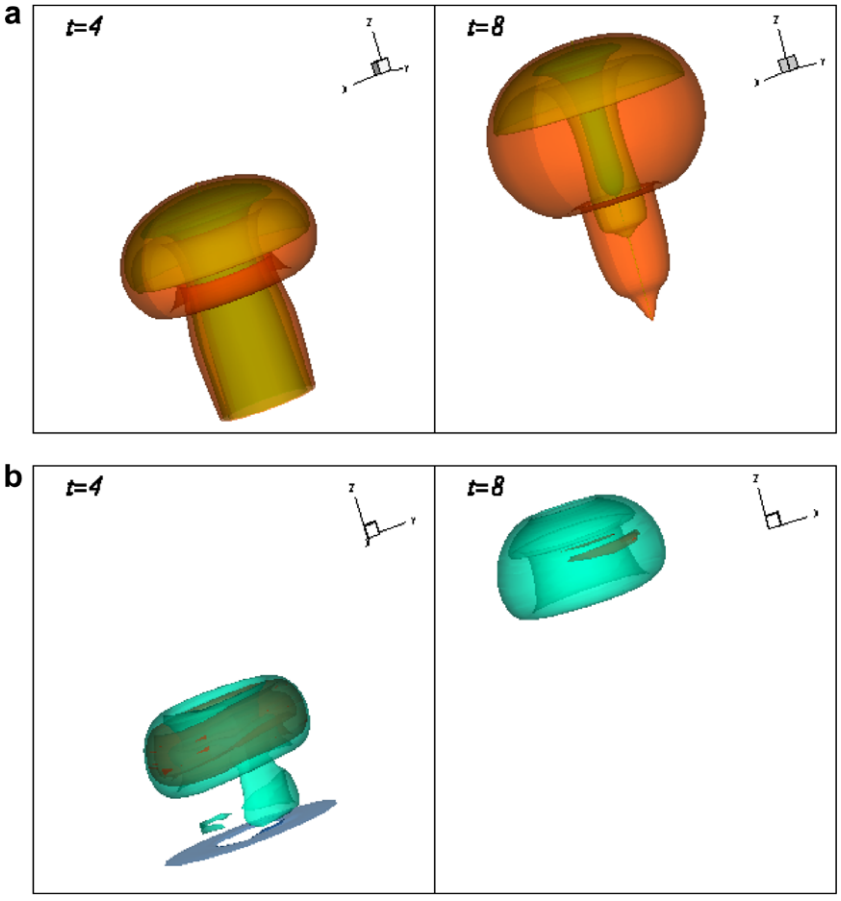

Fig. 2. (a) Surfaces of constant temperature for an axisymmetric cold jet ($\alpha = 2$, $Re = 1000$). (b) Surfaces of constant vorticity for a 3-D hot jet with azimuthal random perturbation ($\alpha = 1/2$, $Re = 1000$).

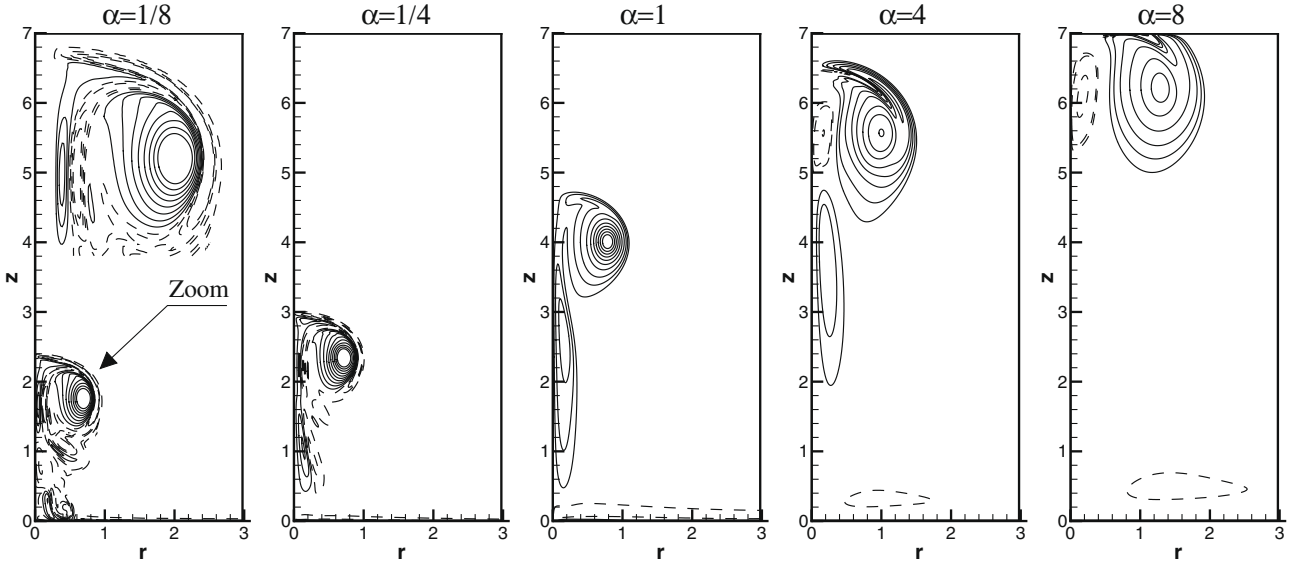

Fig. 3. Instantaneous vorticity contours for different density ratios at $t = 10$ and $Re = 1000$.

be seen in Fig. 4a that the minimum velocities are more pronounced for hot jets than for cold jets.

The variations of the azimuthal vorticity (Fig. 4b) show clearly the complex flow structure of the vortex ring, especially for hot jets. The main clockwise-rotating cell lies between two small counter-rotating cells corresponding to the two minima in the streamwise velocity profiles for the hot jet. In the case of an isothermal jet (incompressible case) the fluid rotates everywhere in the clockwise direction with a cell attached to the symmetry axis. For cold jets, the leading vortex moves away from the axis and the rotation

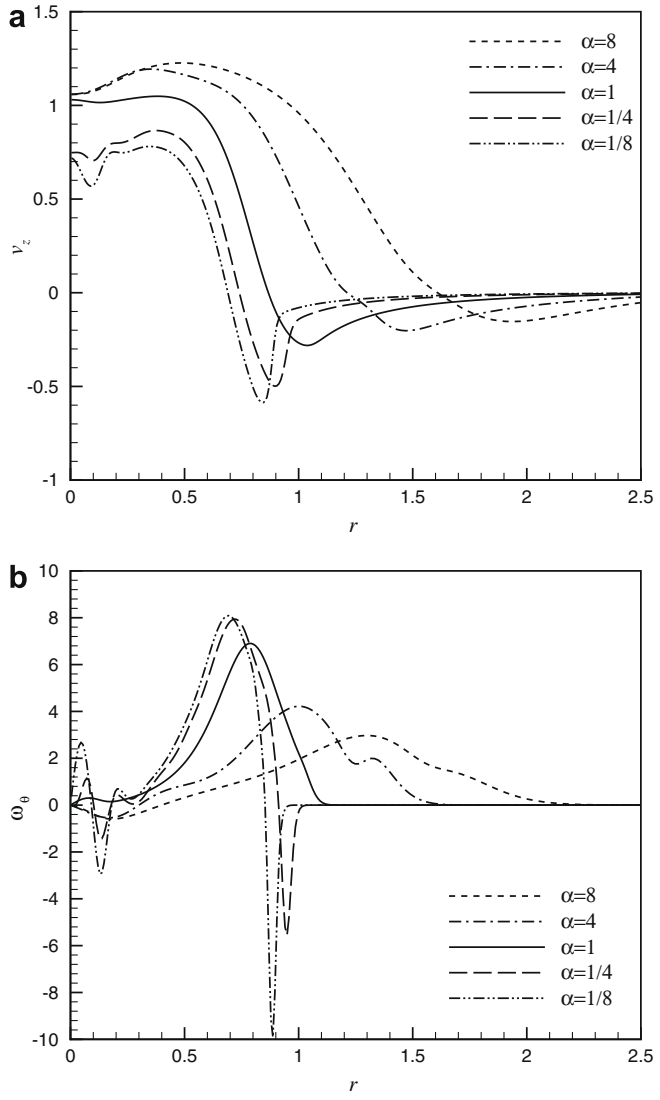

Fig. 4. Radial profiles for different density ratios at $t = 10$; (a) axial velocity, (b) vorticity.

speeds are much less. As the density ratio is increased, a weak counter-rotating cell develops near the axis and the flow structure becomes less complex than for hot jets.

4.2.2. Density fields

The instantaneous isocontours of density obtained for different ratios $\alpha = (1/4, 1, 4)$ are shown in Fig. 5. The plots allow comparison of the density fields after the shut-off of the injection for *Re* = 750 and *Re* = 1500 and at various times corresponding to the same downstream position of the front jet, approximately equal to 5.5 diameters. The influence of the density ratio α is clearly seen on the topology of the jet. In the case of cold jets, a bulky vortex ring develops and the trailing flow, which is not absorbed into the vortex, remains concentrated around the axis and moves far downstream of the orifice exit. On the other hand, for the hot jet, vortices develop in the trailing shear layer which spreads out in front of the orifice exit. These instabilities are all the more amplified since the heated jet temperature is increased. Comparisons with *Re* = 750 show that the jet front is less advanced. The leading vortex is a little bigger for all the injection cases and the instabilities of the hot jet are less developed.

In order to examine the differences between the features of hot and cold jets, the density profiles along a section through the center of the vortex are shown in Fig. 6 for various times during the evolution of the vortex ring. The curves in Fig. 6a show that around the axis the density within the jet ($\alpha = 8$) remains equal to that of the cold injected fluid while it starts to decrease at radial positions of the order of the orifice radius. Within the vortex core, the density takes smaller values which are close to that of the ambient fluid. The hot jet density ($\alpha = 1/8$) evolves in a different way (Fig. 6b). During the discharge period ($t \leqslant 3$), the density for $r < 0.5$ has a minimum value equal to the injected fluid one and slightly larger values in the vortex core diameter ($0.5 < r < 1$, approximately). Once the injection is stopped, the magnitude of the roll-up is so high that the ambient fluid is entrained toward the axis. Consequently, the density along the axis is close to ambient while the smallest densities are located in the vortex core.

4.2.3. Temperature fields

The evolution of the temperature fields is shown in Fig. 7 in the form of instantaneous maps at different times, during and after fluid injection, for both hot and cold jets with the strong density contrasts $\alpha = 1/8$ and $\alpha = 8$. It is worth noting that the Reynolds number being based on the jet properties, the kinematic viscosity of the surrounding flow is smaller than for the hot jet one by a factor $\alpha^{1+\sigma}$. The opposite is the case for the cold jet since it develops in a hot surrounding.

Fig. 7a shows that the high temperature fluid, initially distributed at the orifice section during the injection, is progressively conveyed towards the vortex ring. At time $t = 11$, the hot fluid is totally trapped into the vortex core while the ambient fluid is led into the axis region. This outcome is quantitatively demonstrated by the temperature distributions at $t = 3$ and $t = 6$ which are plotted in Fig. 7a along a line passing through the computed vortex centre. Moreover, a sort of wake appears in the trailing flow for $t \geqslant 25$ with vortex pairing near the orifice exit, as can be seen in Fig. 7a

Regarding the cold jet, the maps in Fig. 7b show that the colder fluid remains concentrated around the axis while the outer layer in contact with the surroundings is heated. Unlike the hot jet, the temperature values in the vortex core are now intermediate between those of the injected fluid and the ambient one. This result is due to the increase in thermal diffusivity as the temperature increases on account of the assumption of constant Prandtl number. Moreover, the cold jet with larger momentum leaves the computational domain faster when the density ratio is increased.

4.2.4. Jet front

In order to quantify the penetration of the jet flow into the ambient fluid, we evaluate the jet front, denoted Z_f, defined at each time-step as the position on the axis where the scaled quantities, density $(\rho - \rho_a)/(\rho_j - \rho_a)$ (or temperature) $(T - T_a)/(T_j - T_a)$, are equal to 0.5.

The time evolution of the jet front, Z_f, is shown for various values of the density ratio and for *Re* = 750 and *Re* = 1500 in Fig. 8a. Except during the initial development, the curves for cold and isothermal fluid display a linear evolution with an increase in the slope with α. For hot jets, the slope is reduced once the injection is stopped ($t > 4$). As expected, the cold jet evolving into a surroundings of lower density, travels much faster and spreads all the more quickly as α increases. On the other hand, the more viscous heated jets penetrate into the surroundings more slowly, especially for $\alpha = 1/8$. The effect of the Reynolds number is only noticeable for cold jets during the post-formation phase. It can be seen in Fig. 8a that Z_f slightly decreases for *Re* = 750 while it is almost independent of *Re* for $\alpha < 1$.

The corresponding jet front velocity, $U_v = dZ_f/dt$, is shown in Fig. 8b. Irrespective of the jet-to-ambient density ratio, the jet front velocities drop considerably at the beginning of the vortex genera-

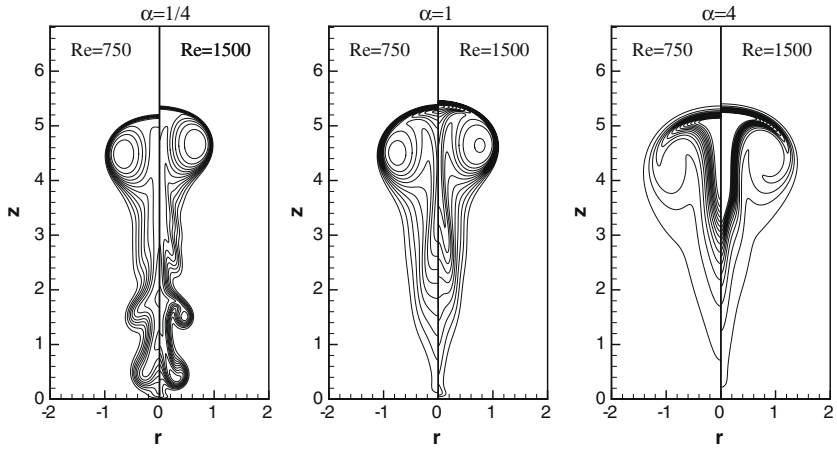

Fig. 5. Instantaneous density contours at $z_f = 5.5$ for two Reynolds numbers and various density ratios; ($\alpha = 1/4, t = 20$), ($\alpha = 1, t = 11.5$) and ($\alpha = 4, t = 8$).

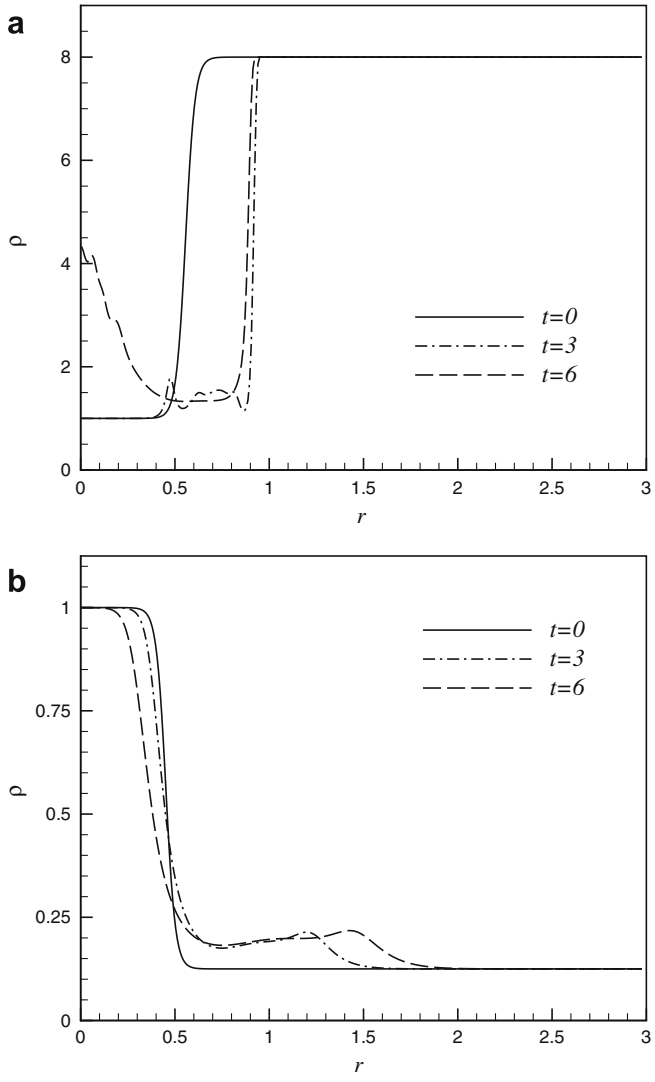

Fig. 6. Density profiles at different times for *Re* = 1000; (a) hot jet ($\alpha = 1/8$), (b) cold jet ($\alpha = 8$).

tion ($t < 2$). They then reach an almost constant value, mainly for cold jets and $t > 4$. Fig. 8b shows that the velocities of the hot jets exhibit a larger drop at the end of the injection program and some fluctuations later on. The effect of the Reynolds number on U_v was found to be very small, even for cold jets.

4.3. Integral characteristics of the vortex ring

Emphasis is placed on the effect of the density ratio on the integral quantities that characterize the vortex ring flows. All these quantities are based on the vorticity distribution ω_θ. The integration is performed over the (r, z) domain at successive instants with a spacing $10\Delta t$. The evolutions of these characteristics are then plotted during the injection phase and there after for $\alpha = (1/8, 1/4, 1, 4, 8)$ and for *Re* = 750 and *Re* = 1500. The comparison is made for $t \leqslant 10$, the time at which the jet with $\alpha = 8$ reaches the exit of the computational domain.

4.3.1. Circulation

The total circulation, defined in Eq. (22), displayed in Fig. 9, presents an almost linear evolution during the injection phase ($t \leqslant 4$) for cold jets. The behavior is different for isothermal and hot jets. The growth rate of the circulation is larger when increasing values of α. The results obtained here are consistent with those reported by Iglesias et al. (2005). The total circulation, in the injection period, remains practically insensitive to the Reynolds number for cold or hot started jets, just as for the incompressible jet (see Gharib et al., 1998). At the end of injection ($t = 4.02$), the circulation decreases abruptly. This effect is more pronounced for hot jets. For $t > 5$ the circulation decays slowly for the isothermal and the hot jet. Conversely, the cold fluid circulations are still rising and finish by stabilizing for a long-time evolution. It should be noticed that the influence of *Re* appears mainly after the end of injection and only for $\alpha \geqslant 1$, so the circulation is larger for *Re* = 1500 while the curves for the hot jet are almost the same. To account for the smaller values of circulation for hot jets in spite of their more intense rotation, we can examine the plots of the vorticity profiles shown in Fig. 4. The positive vorticity is considerably higher compared to that of the cold jet. However, it is in part balanced by the negative vorticity in the ambient flow which leads to smaller values of the overall circulation (Eq. (22)). Concerning the cold jet, even if its vorticity is smaller, this least is shed on much broader region.

4.3.2. Impulse

The hydrodynamic impulse was calculated by using the following expression:

$$\vec{I} = \frac{1}{2}\int_{\Omega} \rho \vec{r} \times \vec{\omega} d\Omega,$$

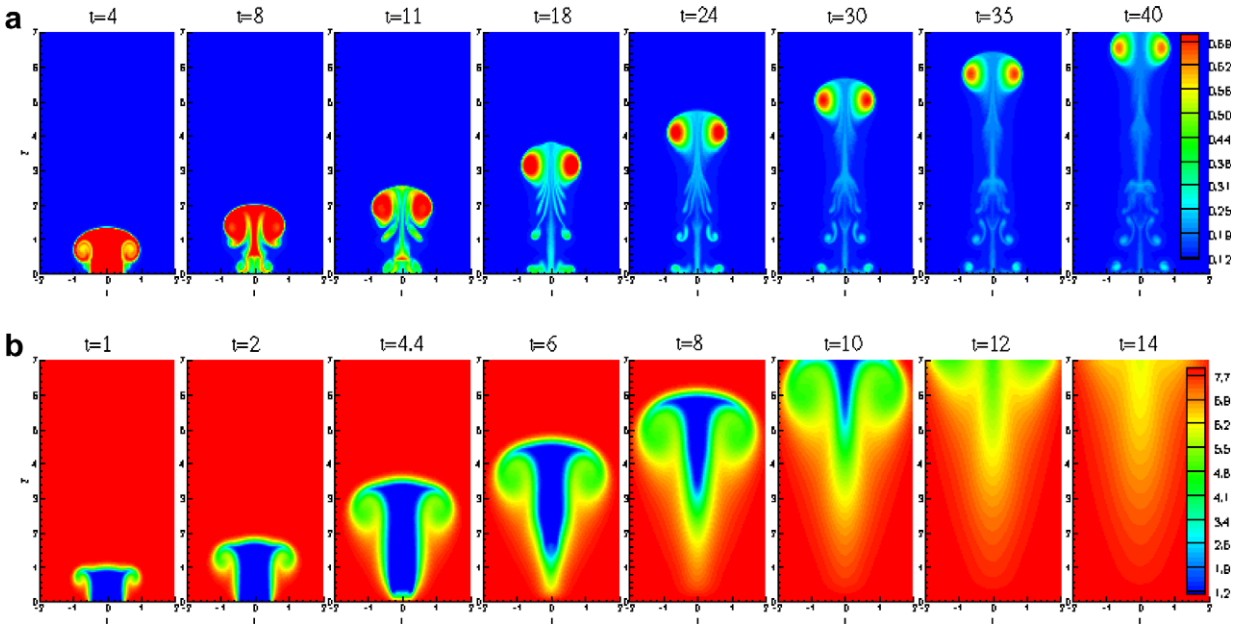

Fig. 7. Instantaneous temperature fields with large density and temperature gradients; (a) hot jet $\alpha = 1/8$, (b) cold jet $\alpha = 8$.

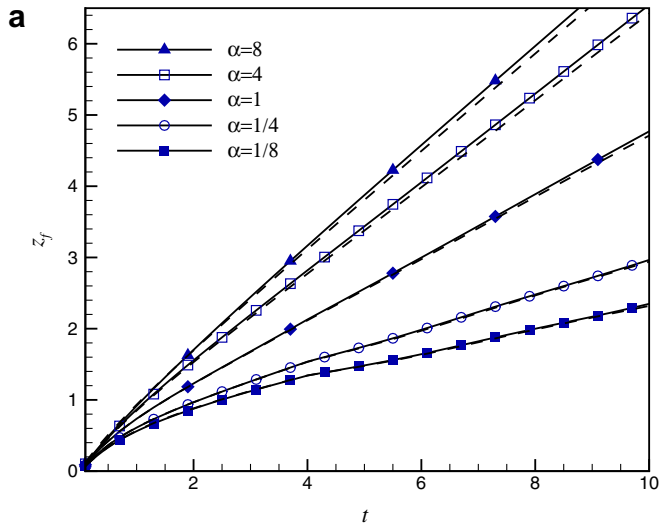

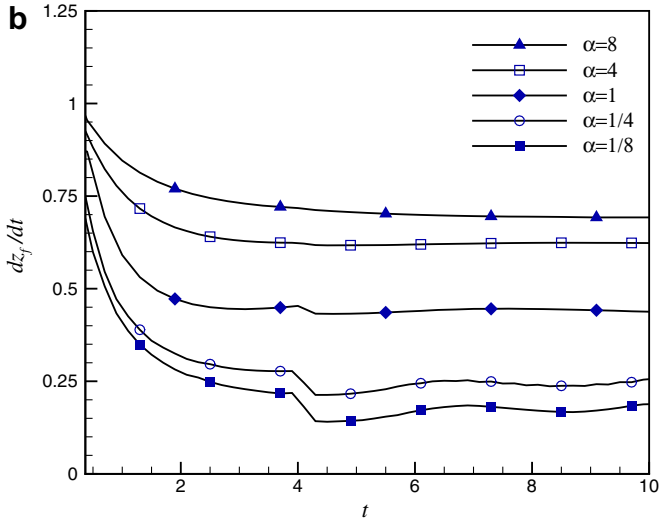

Fig. 8. Time evolution for different density ratios $\alpha = (1/8, 1/4, 1, 4, 8)$, (--- $Re = 750$, —— $Re = 1500$); (a) jet front, (b) velocity of the jet front.

where $\vec{r}$ is the position vector, $\vec{\omega}$ the vorticity vector and $d\Omega$ the volume element. For axisymmetric flow this expression reduces to the streamwise direction component, denoted I, since an axial impulse only is transmitted to the flow field. To separate the density effects from the inertial ones, we focus here on the impulse of the velocity field given by the moment of vorticity

$$I = \pi \int_0^{L_z} \int_0^{L_r} \omega_\theta r^2 \, dr \, dz.$$

It can be observed in Fig. 10, that the temporal increase in the impulse delivered by the vortex is greater for cold jets than for hot jets. Significant growth during the fluid discharge is noticed for $\alpha = 8$. The stop of the injection is marked by an abrupt decay of I for all values of the density ratio α. Then, for $t > 4$, the impulse keeps increasing for $\alpha \geqslant 1$ and it is almost constant for $\alpha < 1$. The large differences between the impulse curves are mainly due to the influence of the vortex sizes in the crosswise direction r. For hot jets, the

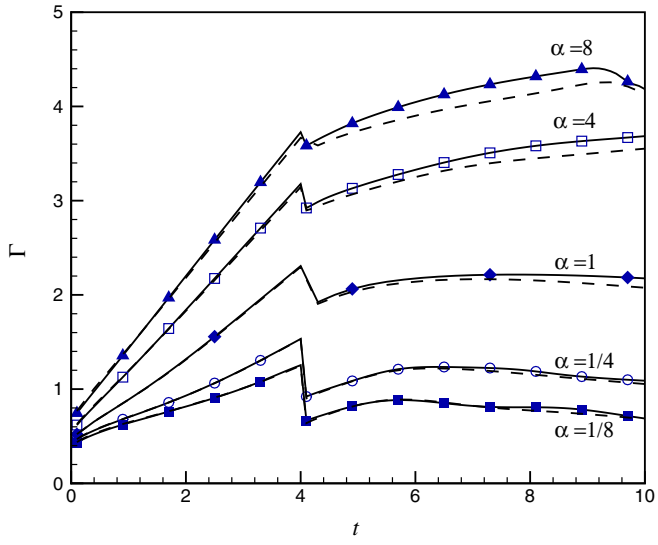

Fig. 9. Time evolutions of the circulation for different density ratios (---$Re = 750$, —— $Re = 1500$).

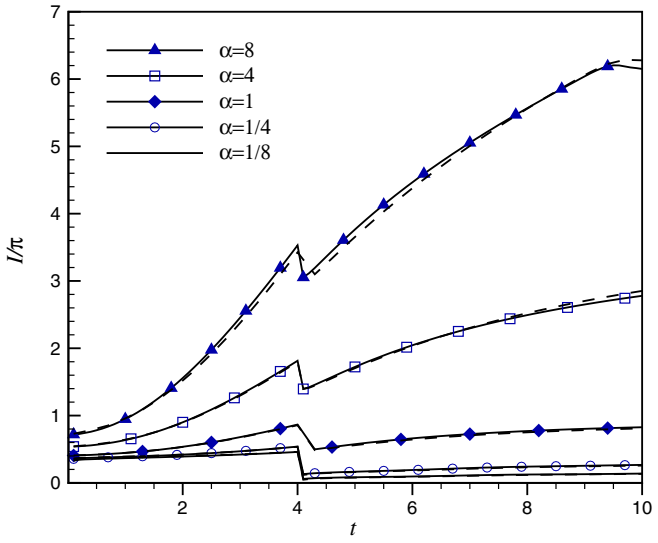

Fig. 10. Time evolutions of the impulse for different density ratios (---$Re = 750$, —– $Re = 1500$).

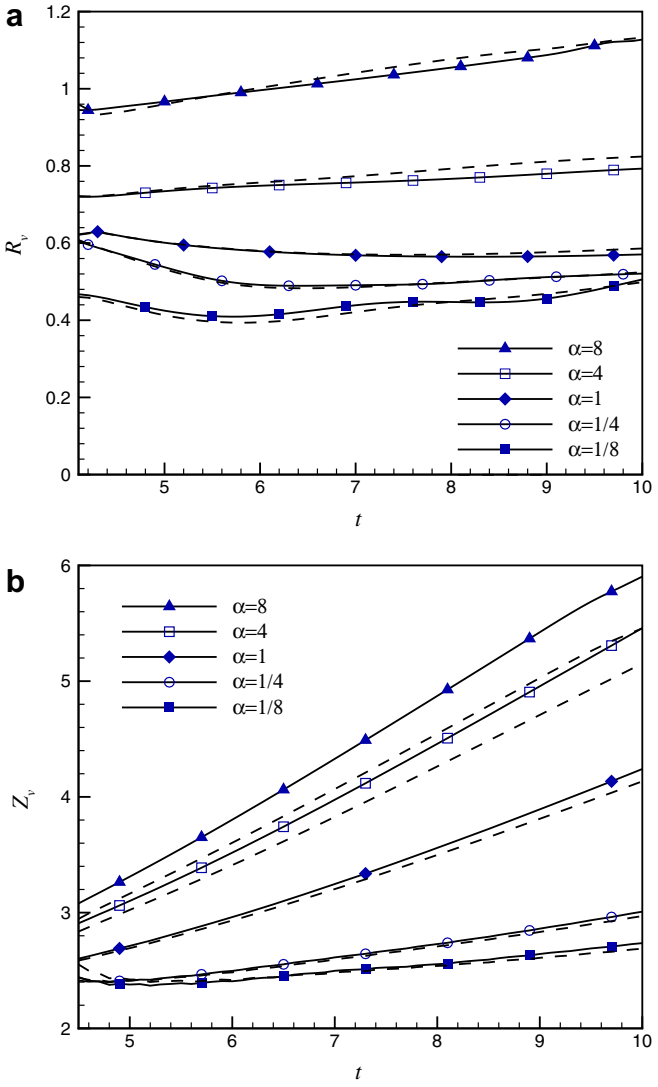

Fig. 11. Time evolutions of the vortex ring kinematics for different density ratios (---$Re = 750$, —– $Re = 1500$); (a) radius, (b) axial position.

vortices are indeed confined in a narrow region in the vicinity of the orifice rim ($0 < r < 0.7$ approximately). Furthermore, the plots show that the differences for $Re = 750$ are quite small, so the invariance of the impulse according to the Reynolds number is also preserved for variable density vortex rings.

4.3.3. Vortex kinematics

The centroid coordinates (Z_v, R_v) of the vortex ring, where Z_v is the streamwise location and R_v is the centroid radius, were defined by Helmholtz (see Saffman, 1992).

$$Z_v = \frac{\int_0^{L_z}\int_0^{L_r} \omega_\theta z r^2 dr dz}{\int_0^{L_z}\int_0^{L_r} \omega_\theta r^2 dr dz}, \quad R_v = \frac{\int_0^{L_z}\int_0^{L_r} \omega_\theta r dr dz}{\int_0^{L_z}\int_0^{L_r} \omega_\theta dr dz}.$$

As can be noted from these expressions, the downstream position Z_v of the centroid is weighted by the hydrodynamic impulse, since the vortex travels in the direction of the given impulse, and the radius R_v is weighted by the circulation. It should be noted that these formulas are available only in the post-formation phase. As for the circulation and the impulse, Fig. 11 shows that the kinematic coordinates Z_v and R_v conserve a similar behavior according to the density ratio with smaller values for hot jets, greater values for cold jets and intermediate values for the isothermal jet. The Reynolds number does not sensibly affect the vortex ring radius (see Fig. 11a) whereas Z_v (Fig. 11b) takes smaller values for $Re = 750$ for isothermal and cold jets, especially when α increases. It should be outlined that of the vortex center coordinates are larger than the centroid ones. This offset is primarily due to the amount of vorticity deposited in the wake of the jet.

5. Conclusion

A computing code for simulating variable density jets and appropriate for dealing with strong density and temperature contrasts was developed. Simulations performed for an impulsive and brief discharge of hot or cold no-buoyant fluid with density ratios ranging from 1/8 to 8 allowed to describe the jet flow dynamics and thermals. Results show that the common feature between all injection cases is the formation, at the head of the flow, of a leading vortex ring. However, the flow behavior is different depending on whether the injected fluid is hotter or colder than the ambient one. Hot jets exhibit more intense roll-up of the vortex ring which is surrounded by a counter-rotating layer. This effect is due to the baroclinic torque and is accentuated when the density contrast increases. The results on the temperature field is that the hot injected fluid is trapped into the vortex core while the cold ambient fluid is entrained toward the axis. For a cold fluid injection, voluminous vortex rings are generated and their vorticity is as small as the density ratio is high. The reason is that the cold injected fluid remains concentrated around the axis when the outer layer, including the vortex, is heated by increases in thermal diffusion. The influence of the jet-to-ambient density ratio, α, on the evolution of the vortex ring characteristics, namely circulation, jet front, impulse and kinematics, is analyzed. These quantities, based on the integration of the vorticity fields over the whole domain, are found to increase when increasing α despite the larger values of vorticity for hotter jets. This is due to the occurrence of counter-rotating surrounding flow for hot fluid injection.

References

Benteboula, S., 2006. Résolution des équations de Navier–Stokes à faible nombre de Mach – application à l'étude de l'anneau de vorticité à masse volumique variable. Ph.D. thesis, Université Paris-Est de Marne-la-Vallée. <http://tel.archives-ouvertes.fr/tel-00327102/fr/>.

Boersma, B.J., Brethouwer, G., Nieuwstadt, F.T.M., 1998. A numerical investigation on the effect of the inflow conditions on the self similar region of the jet. Phys. Fluids 10, 899–909.

Cook, A.W., Riley, J.J., 1996. Direct numerical simulation of a turbulent reactive plume on a parallel computer. J. Comput. Phys. 129, 263–283.
Dabiri, J.O., Gharib, M., 2004. Delay of vortex ring pinch-off by an imposed bulk counterflow. Phys. Fluids 16, L28–L30.
Didden, N., 1979. On the formation of vortex ring: rolling-up and production of circulation. J. Appl. Math. Phys 30, 101–116.
Gharib, M., Rambod, E., Shariff, K., 1998. A universal time scale for vortex ring formation. J. Fluid Mech. 360, 121–140.
Guillard, H., Viozat, C., 1999. On the behaviour of upwind schemes in the low Mach number limit. Comput. Fluids 28, 63–86.
Glezer, A., 1988. The formation of vortex rings. Phys. Fluids 31, 3532–3542.
Harten, A., 1983. High resolution schemes for hyperbolic conservation laws. J. Comput. Phys. 49 (3), 357–393.
Iglesias, I., Vera, M., Antonio, L.S., 2005. Simulations of starting gas jets at low Mach numbers. Phys. Fluids 17, 038105.
James, S., Madnia, C.K., 1996. Direct numerical simulation of a laminar vortex ring. Phys. Fluids 8, 2400.
Klein, R., 1995. Semi-implicit extension of a godunov-type scheme on low Mach number asymptotics. J. Comput. Phys. 121, 213.
Lim, T.T., Nickels, T.B., 1995. Vortices in Fluid Flows. In: Vortex rings. Kluwer.
Majda, A., Sethian, J., 1985. The derivation and numerical solution of the equation for zero Mach number combustion. Combust. Sci. Technol. 42, 185.
Maxworthy, T., 1977. Some experimental studies of vortex rings. J. Fluid Mech. 81, 465–495.
Michalke, A., 1984. Survey on jet instability theory. Prog. Aerospace Sci. 21, 159.
Müller, B., 1998. Low Mach number asymptotics of the Navier–Stokes equations. J. Eng. Math. 34, 97–109.
Munz, CD., Roller, S., Klein, R., Geratz, KJ., 2003. The extension of incompressible flow solvers to the weakly compressible regime. Comput. Fluids 32, 173–196.
Najm, H.N., Wyckoff, P., Knio, O.M., 1998. A semi-implicit numerical scheme for reacting flow. J. Comput. Phys. 143, 381.
Nicoud, F., 2000. Conservative high-order finite-difference scheme for low-Mach number flows. J. Comput. Phys. 158, 71–97.
Orlanski, I., 1976. A simple boundary condition for unbounded hyperbolic flows. J. Comput. Phys. 21, 251.
Pember, R.B., Bell, A.S., Collela, J.B., Howell, P., Lai, M., 1996. A higher order projection method for the simulation of unsteady turbulent non premixed combustion in an industrial burner. Transport Phenom. Combust., 1200–1211.
Pullin, D.I., 1979. Vortex ring formation at tube and orifice openings. Phys. Fluids 22, 401.
Roller, S., Munz, C.-D., 2000. A low Mach number scheme based on multi-scale asymptotics. Comput. Visual. Sci. 3 (1/2 500), 85–91.
Saffman, P.G., 1978. The number of waves on unstable vortex rings. J. Fluid Mech. 84, 625.
Saffman, P.G., 1992. Vortex dynamics. Cambridge Monographs on Mechanics and Applied Mathematics. Cambridge University Press, Cambridge, NY.
Shariff, K., Leonard, A., 1992. Vortex rings. Ann. Rev. Fluid Mech. 24, 235–279.
Turkel, E., 1987. Preconditioning methods for solving the incompressible and low speed compressible equations. J. Comput. Phys. 72, 277–298.
Verzicco, R., Orlandi, P., 1995. Mixedness in the formation of a vortex ring. Phys. Fluids 7, 1513.
Verzicco, R., Orlandi, P., 1996. A finite-difference scheme for three-dimensional incompressible flows in cylindrical coordinates. J. Comput. Phys. 123, 402.
Vreugenhil, C.B., Koren, B., 1993. Numerical Methods for Advection–Diffusion Problems, vol. 45. Vieweg, Braunschweig.
Zhao, W., Steven, H.F., Mongeau, L.G., 2000. Effects of trailing jet instability on vortex ring formation. Phys. Fluids 12, 589.